Revision_1

Elastic behaviour and phase stability of pyrophyllite and talc at high pressure and temperature

G. Diego Gatta, Paolo Lotti, Marco Merlini, Hanns-Peter Liermann, Andrea Lausi, Giovanni Valdrè, Alessandro Pavese

Running title: H*P*-H*T* behaviour of pyrophyllite and talc

Abstract

Introduction

Experimental methods

Results: Behaviour of pyrophyllite at high pressure

Results: Behaviour of pyrophyllite and talc at high temperature

Discussion and conclusions

Acknowledgements

References

Figures/Tables

Corresponding author: G. Diego GATTA

Dip. Scienze della Terra
Universita' degli Studi di Milano
Via Botticelli, 23
I-20133 Milano, Italy
Tel. +39 02 503 15607
Fax +39 02 503 15597
E-Mail: diego.gatta@unimi.it

Operating system: Windows XP

(To be submitted to *Physics and Chemistry of Minerals*)

Elastic behaviour and phase stability of pyrophyllite and talc at high pressure and temperature

[1,2] G. Diego Gatta, [1]Paolo Lotti, [1]Marco Merlini, [3]Hanns-Peter Liermann, [4]Andrea Lausi, [5]Giovanni Valdrè, [1]Alessandro Pavese

[1]Dipartimento di Scienze della Terra, Università degli Studi di Milano, Via Botticelli 23, I-20133 Milano, Italy
[2]CNR - Istituto di Cristallografia, Sede di Bari, Via G. Amendola 122/o, Bari, Italy
[3] Photon Sciences, DESY, Notkestr. 85, D-22607 Hamburg, Germany
[4]Elettra - Sincrotrone Trieste S.C.p.A., Strada Statale 14 - km 163.5, I-34149 Basovizza, Trieste, Italy
[5] Dipartimento di Scienze Biologiche, Geologiche a Ambientali, Università di Bologna, Piazza di Porta San Donato 1, I-40126, Bologna, Italy

Abstract

The compressional behaviour of (triclinic) pyrophyllite-1*Tc* was investigated by means of in-situ synchrotron single-crystal diffraction up to 6.2 GPa (at room temperature) using a diamond anvil cell. Its thermal behaviour was investigated by in-situ synchrotron powder diffraction up to 923 K (at room pressure) with a furnace. No evidence of phase transition has been observed within the pressure-range investigated. The α angle decreases whereas the β and γ angles increase with *P*, with the following linear trends: $\alpha(P) = \alpha_0 - 0.203(9)\cdot\Delta P$, $\beta(P) = \beta_0 + 0.126(8)\cdot\Delta P$, and $\gamma(P) = \gamma_0 + 0.109(5)\cdot\Delta P$ (angles in ° and *P* in GPa). *P*-*V* data fits with isothermal Murnaghan and third-order Birch-Murnaghan Equations of State yield: K_{T0}= 47(3) GPa and *K'* = 6.6(14) for the M-EoS fit, K_{T0}= 47(4) GPa and *K'* = 7.3(19) for a III-BM-EoS fit, with the following anisotropic compressional scheme: $\beta_a : \beta_b : \beta_c = 1.06 : 1 : 4.00$. The evolution of the "Eulerian finite strain" *vs* "normalized stress" leads to: *Fe*(0) = 47(3) GPa as intercept value and regression line slope with *K'* = 7.1(18). A drastic and irreversible change of the thermal behaviour of pyrophyllite-1*Tc* was observed at 700<*T*<850 K, likely ascribable to the first stage of the *T*-induced de-hydroxylation. Between 298 and 700 K, the α angle shows a slight decrease whereas the β and γ angles tend to be unaffected in response to the applied temperature; all the unit-cell edges show a monotonic increase. The axial and volume thermal-expansion coefficients of pyrophyllite were modelled between 298 and 773 K following the equation $\alpha_V(T) = \alpha_0(1\text{-}10T^{-1/2})$, with $\alpha_{V298K} = 2.2(2)\cdot10^{-5}$ K^{-1} (with V_0 = 424.2(1)Å^3 and $\alpha_0 = 5.5(3)\cdot10^{-5}$ K^{-1}) and thermal anisotropic scheme α_a: α_b: α_c = 1.20 : 1 : 2.72. By linear regression, we obtained: $V(T)/V_0 = 1 + \alpha_{0V}\cdot T = 1 + 3.1(2)\cdot10^{-5}\cdot\Delta T$.

The thermal behaviour of talc-1*Tc* was investigated by in-situ synchrotron powder diffraction up to 1173 K (at room-*P*) with a furnace. At 423 K, the diffraction pattern was indexable with a monoclinic unit-cell but with a doubling of the *c*-axis (as expected for the 2*M*-polytype). At *T* >

1123 K, an irreversible transformation occurs, likely ascribable to the first stage of the *T*-induced de-hydroxylation. Between 423 and 1123 K, the β angle decreases in response to the applied temperature; all the unit-cell edges show a monotonic increase. The volume expansion coefficient of talc was modelled between 423 and 1123 K by the linear regression, yielding: $V(T)/V_0 = 1 + \alpha_{0V} \cdot T = 1 + 2.15(3) \cdot 10^{-5} \cdot \Delta T$.

The comparative elastic analysis of pyrophyllite and talc, using the data obtained in this and in previous studies, shows that pyrophyllite is more compressible and more expandable than talc.

Keywords: pyrophyllite, talc, synchrotron diffraction, high-pressure, high temperature, compressibility, expansivity.

Introduction

Pyrophyllite and talc are phyllosilicates with ideal chemical formula $Al_2Si_4O_{10}(OH)_2$ and $Mg_3Si_4O_{10}(OH)_2$ (Bailey 1988), respectively. Pyrophyllite usually occurs in low-grade metamorphosed sediments or in high-pressure/low-temperature metamorphic rocks (*e.g.*, ~ 0.8 GPa, 570 K, Theye et al. 1997) significantly rich in Al. Very aluminous metapelites, metabauxites or rocks enriched in Al by base-leaching during hydrothermal alteration can contain pyrophyllite. Kaolinite, in contrast, is the Al-rich phyllosilicate usually occurring in sediments. The phase stability of pyrophyllite, deduced on the basis of thermodynamic data, is up to a maximum of ~2 GPa and 713 K (Theye et al. 1997). Talc is a natural product of metamorphism or hydrothermal alteration of Mg-rich ultramafic rocks (Evans and Guggenheim 1988). In serpentinized peridotites, for example, talc usually occurs. In response to applied *P/T*, metasediments involved in subduction processes are expected to transform to a talc-bearing assemblage (*e.g.* Mysen et al. 1998). Talc contains ~5 wt% of H_2O, and so several studies have been devoted to the potential role played by this phyllosilicate as a "vector" of water into the mantle via subduction zones (*e.g.* Poli and Schmidt 2002, and reference therein). The decomposition of talc to coesite + enstatite + H_2O was observed at 3-5 GPa and 970-1070 K (Pawley and Wood 1995).

Pyrophyllite and talc are also important industrial minerals, mainly because of their low coefficient of friction, chemical inertness and thermal stability. These two phyllosilicates act as functional and high-performance mineral additives. They are widely used in several technological applications: paper coating, paint, ceramics, polymer industries, joint compounds, and pharmaceuticals. The industrial applications of talc, for example, led to series of studies of its deformational behavior by compaction and shear, even at high temperature (*e.g.* Dellisanti and

Valdrè 2008, 2010; Dellisanti et al. 2009). World talc + pyrophyllite production in 2012 was estimated to be 7,600,000 tons; China was the main producer with 2,200,000 tons.

The crystal structure of talc and pyrophyllite consists of a sheet of linked 3·[$MgO_4(OH)_2$] or 2·[$AlO_4(OH)_2$] octahedra ("O"), respectively, sandwiched between two sheets of SiO_4 tetrahedra ("T") combined to six-member rings, giving the so-called "T-O-T" layered structure (Fig. 1). The charge-neutral T-O-T layers are held together by relatively weak van der Waals attractive forces, leading to the extreme softness of these phyllosilicates along a direction perpendicular to the T-O-T layers. Crystals of talc and pyrophyllite are affected by polytypism and stacking disorder, as often observed in phyllosilicates (*e.g.*, Lee and Guggenheim 1981 and references therein; Ďurovič and Weiss 1983; Weiss and Ďurovič 1984).

Despite the important role played by pyrophyllite and talc in petrological or industrial processes, several questions about the crystal chemistry and the thermodynamic properties of these minerals are still unanswered. Conflicting results are available in the literature about the high-pressure (H*P*) and -temperature (H*T*) behaviour of pyrophyllite and talc. In the studies previously performed, the polytypic nature of the two phyllosilicates is often not mentioned and, in addition, the quality of the data is far from the modern standards. Recently, Gatta et al. (2013) reinvestigated the crystal structure of the 1*Tc* (or 1*A*) polytype of talc by single-crystal X-ray and neutron diffraction and its high-pressure behavior by in-situ single-crystal X-ray diffraction up to 16 GPa, providing also a critical review of the elastic behaviour of talc on the basis of the data previously reported. The experimental findings of Gatta et al. (2013) were recently corroborated by quantum mechanical simulations of talc compression up to 10 GPa and second-order elastic constants reported by Ulian et al. (2014). The thermal expansivity of talc was measured by Pawley et al. (1995) by in-situ X-ray powder diffraction (in home-lab) up to 1080 K. The only experimental data on the compressibility of pyrophyllite have been reported by Pawley et al. (2002), on the basis of in-situ synchrotron energy-dispersive powder diffraction in a multi-anvil apparatus collected up to ~ 6 GPa. Pawley et al. (2002) reported also the thermal expansivity of pyrophyllite, based on the experimental data of the Bachelor Thesis of Symmes (1986). The expansivity of pyrophyllite appears to be slightly greater than that of talc (Pawley et al. 2002), though a comparison of the data was somehow hindered by the different quality and collection protocols. In this light, the aims of this study are: 1) a reinvestigation of the compressional behaviour of pyrophyllite, by in-situ single-crystal synchrotron diffraction with a diamond anvil cell, and 2) a reinvestigation of the high-temperature behaviour of pyrophyllite and talc by in-situ synchrotron powder diffraction with a furnace. This will allow us to perform a comparative thermo-elastic analysis of pyrophyllite and talc and to provide high-quality compressional and thermal parameters.

Experimental methods

Natural samples of pyrophyllite from Tres Cerritos, Mariposa County (California, USA)), and talc from the metamorphic complex of Val di Vizze (Pfitschtal), Trentino-Alto Adige (Südtirol, Italy), were used in this study.

Electron microprobe analysis of talc in wavelength dispersive mode (EPMA-WDS) was reported by Gatta et al. (2013), with the following chemical formula: $(Mg_{2.93}Fe_{0.06})_{\Sigma 2.99}(Al_{0.02}Si_{3.97})_{\Sigma 3.99}O_{10}(OH)_{2.10}$. EPMA-WDS analysis was performed on several crystals of pyrophyllite (optically free of defects or zoning) using a Jeol JXA-8200 microprobe. Major and minor elements were determined at 15 kV accelerating voltage and 10 nA beam current with a counting time of 20 seconds. The standards employed were: albite (Al, Si, Na), microcline (K), anorthite (Ca), fayalite (Fe), and forsterite (Mg). The crystals appear to be chemically homogeneous and averaging 10 points analyses we obtained: SiO_2 65.80 wt%, Al_2O_3 28.46 wt%, FeO 0.14 wt%, and H_2O 6.70 wt% (by difference), resulting in the following chemical formula: $(Al_{1.94}Fe_{0.01})_{\Sigma 1.95}(Al_{0.07}Si_{3.93})_{\Sigma 4}O_{10}(OH)_{2.2}$ (Mg, Na, K, and Ca fraction negligible).

The H*P*-synchrotron X-ray single-crystal diffraction experiment on pyrophyllite was performed at the beamline P02.2 (Extreme Conditions Beamline) at DESY/PETRA III, using X-rays with an energy of 42.7 keV (0.29036 Å wavelength) and a focusing spot of ~ 8.5 (H) x 1.8 (V) μm^2 originating from a Compound Refractive Lenses (CRL) system consisting of 120 Be lenses with a radius of 50 µm (400 µm beam acceptance) and a focal length of 1221 mm. A platy crystal of pyrophyllite was loaded in a symmetric diamond anvil cell (DAC), equipped with Boehler Almax design diamonds/seats with a 70° opening and 300 µm culets size (Boehler and De Hantsetters 2004). The cleavage of pyrophyllite on {001} allowed one orientation only, with the *ab*-plane perpendicular to the DAC axis. A crystal, exhibiting a low degree of stacking disorder, was selected for the high-pressure experiment. A 250 µm thick steel gasket was pre-indented to 50 µm and then drilled with 200 µm hole, in which the crystal of pyrophyllite, along with some calibrated ruby spheres for pressure determination (by ruby-fluorescence method, Mao et al. 1986), were located. A mix of methanol:ethanol = 4:1 was used as hydrostatic pressure transmitting medium up to 10 GPa (Angel et al. 2007). Pressure was increased with an automated pressure driven system and measured with the online ruby/alignment system. Diffraction patterns were acquired on a PerkinElmer XRD 1621 flat panel detector, using an in house script for collecting step-scan diffraction images. Sample to detector distance (402.3 mm) was calibrated using a CeO_2 standard (NIST 674a). The diffraction data were collected up to 6.2 GPa with a pure ω-scan ($-28 \leq \omega \leq +28°$), step size of 1° and an exposure time of 5 s/frame (see Rothkirch et al 2013 for further details). At $P > 7$ GPa, the crystal was irreversibly damaged by the diamonds. The images were converted with an in-house software

script (Rothkirch et al. 2013) to conform to the "Esperanto" format of the program CrysAlis (Agilent 2012). Bragg peaks collected at room-*P* were indexed with a metrically triclinic unit-cell (with a = 5.179(1), b = 8.981(1), c = 9.377(8) Å, α = 90.97(4), β = 100.94(5), γ = 89.87(2)°; reflection conditions consistent with those of the space group $C\bar{1}$) and their intensities were integrated and corrected for Lorentz-polarization (Lp) effects, using the CrysAlis package (Agilent 2012). Any attempt at performing a structure refinement was unsuccessful. The unit-cell parameters at room and high pressure were refined with the program *UnitCell* (Holland and Redfern 1997) on the basis of the inter-planar distances extracted by CrysAlis (Table 1). No evidence of phase transition was observed within the *P*-range investigated.

In-situ H*T* data of pyrophyllite and talc were collected at the MCX beamline at ELETTRA (Trieste, Italy), using the high resolution diffractometer available at the station. The sample was contained in quartz capillary, to reduce preferred orientation effects. High temperature was maintained with a hot air blower device, and temperature was monitored with a thermocouple and calibrated against H*T* thermal expansion and phase transition of quartz. Monochromatic radiation (λ = 0.8202 Å) was used. All attempts to refine the crystal structure of pyrophyllite and talc at high temperature by Rietveld method (Rietveld 1969) were unsuccessful, likely due to the poor random orientation of crystallites in the capillary (due to the layered nature of the samples), to the absence of heavy atoms and to the low symmetry of the structures. The diffraction patterns at high temperature were then treated by Le Bail full-profile fit (Le Bail et al. 1988), using the GSAS package (Larson and Von Dreele 1994), aimed to obtain the unit-cell parameters only. All diffraction patterns were fitted using the pseudo-Voigt profile function of Thomson et al. (1987); the background curves were modelled with a Chebyshev polynomial. The refined unit-cell parameters of pyrophyllite and talc at high temperature are listed in Table 1.

Results: Behaviour of pyrophyllite at high pressure

The evolution of the unit-cell parameters of pyrophyllite in response to the applied pressure (data listed in Table 1) is shown in Fig. 2. The compressional patterns do not show any clear evidence of phase transition within the *P*-range investigated. The α angle decreases whereas the β and γ angles increase with *P*, with the following linear trends: $\alpha(P) = \alpha_0 - 0.203(9)\cdot\Delta P$, $\beta(P) = \beta_0 + 0.126(8)\cdot\Delta P$, and $\gamma(P) = \gamma_0 + 0.109(5)\cdot\Delta P$ (angles in ° and *P* in GPa). This leads to a distortion of the unit-cell in response to hydrostatic pressure (Fig. 2).

The evolution of the "Eulerian finite strain" *vs* "normalized stress" (*fe-Fe* plot; Angel 2000) is shown in Fig. 2. The intercept value obtained by a weighted linear regression through the data points is $Fe(0)$ = 47(3) GPa, the slope of the regression line leads to a K' value of 7.1(18). Unit-cell

volumes *vs.* *P* were fitted with a Murnaghan (M-EoS) and with a second and third-order Birch-Murnaghan Equations of State (II- and III-BM-EoS) (Murnaghan 1937; Birch 1947) using the EOS-FIT program (Angel 2000). The least-squares fit was performed using the data weighted by the uncertainties in *P* and *V*. The refined elastic parameters are: V_0 = 428.3(5) Å^3, K_{T0} = 47(3) GPa and *K'* = 6.6(14) for the M-EoS fit, V_0= 427.9(4) Å^3 and K_{T0}= 54(1) GPa for the II-BM-EoS fit, and V_0= 428.3(5) Å^3, K_{T0}= 47(4) GPa and *K'* = 7.3(19) for a III-BM-EoS fit, respectively.

The axial compressibilities were calculated using the "linearized" II-BM-EoS (Angel 2000). The least-squares fits were performed accounting for uncertainties in *P* and length. The refined elastic parameters are: a_0 = 5.179(3) Å and $K_{T0}(a)$ = 99(6) GPa for the *a*-axis; b_0 = 8.981(2) Å and $K_{T0}(b)$ = 104(3) GPa for the *b*-axis; c_0 = 9.377(13) Å and $K_{T0}(c)$ = 26(1) GPa for the *c*-axis [$\beta(a) = 1/3K_{T0}(a)$ = 0.0034(2) GPa^{-1}; $\beta(b) = 1/3K_{T0}(b)$ = 0.0032(1) GPa^{-1}; $\beta(c) = 1/3K_{T0}(c)$ = 0.0128(4) GPa^{-1}; anisotropic scheme $\beta(a) : \beta(b) : \beta(c)$ = 1.06 : 1 : 4.00].

The magnitude and orientation of the principal unit-strain coefficients between room pressure and the maximum *P* achieved (ΔP = 6.18 GPa), derived on the basis of the finite Eulerian strain tensor, were calculated with the *Win_Strain* software (Angel 2011). We have chosen the following Cartesian axial system: *x*//*a** and *z*//*c*. The strain ellipsoid is oriented as follows: ε_3 = -0.059(1) GPa^{-1}, ε_2 = -0.0233(5) GPa^{-1}, and ε_1 = -0.0104(5)GPa^{-1} (with $|\varepsilon_3| > |\varepsilon_2| > |\varepsilon_1|$); $\varepsilon_1 \angle a$ = 52(1)°, $\varepsilon_1 \angle b$ = 140(1)°, and $\varepsilon_1 \angle c$ = 108.6(8)°; $\varepsilon_2 \angle a$ = 142(1)°, $\varepsilon_2 \angle b$ = 127(2)°, and $\varepsilon_2 \angle c$ = 87.3(9); $\varepsilon_3 \angle a$ = 88(1)°, $\varepsilon_3 \angle b$ = 103(1)°, and $\varepsilon_3 \angle c$ = 19(1)°. The orientation of the strain ellipsoid is shown in Fig. 1. The elastic anisotropy of pyrophyllite described on the basis of the unit-strain coefficients between 0.0001 and 6.18 GPa is significant, with $\varepsilon_1 : \varepsilon_2 : \varepsilon_3$ = 1 : 2.24 : 5.67.

Results: Behaviour of pyrophyllite and talc at high temperature

The behaviour of the unit-cell parameters of pyrophyllite with *T* is shown in Fig. 3. A drastic and irreversible change of the thermal behaviour is observed at 700<*T*<850 K, likely ascribable to the first stage of the *T*-induced de-hydroxylation. Between 298 and 700 K, the α angle shows a slight decrease whereas the β and γ angles tend to be unaffected in response to the applied temperature; all the unit-cell edges show a monotonic increase. The axial and volume thermal-expansion coefficients of pyrophyllite were then modelled between 298 and 773 K following the protocol of Pawley et al. (1996) and Holland and Powell (1998). The volume thermal expansion coefficient, $\alpha(T)$, is defined as:

$$\alpha_V(T)=(1/V)(\partial V/\partial T)= \partial \ln V/\partial T.$$

The evolution of α with T can be described by the polynomial function:

$$\alpha_V(T) = \alpha_0 - \alpha_1 T^{-1/2}.$$

The two aforementioned equations lead to:

$$V(T) = V_0\exp[\alpha_0(T-T_0) - 2\alpha_1(T^{1/2}-T_0^{1/2})] \approx V_0[1 + \alpha_0(T-T_0) - 2\alpha_1(T^{1/2}-T_0^{1/2})].$$

Pawley et al. (1996) showed that $\alpha_1 \approx 10\alpha_0$, thus suggesting a simplified form of the previous equations to:

$$\alpha_V(T) = \alpha_0(1-10T^{-1/2}) \text{ and}$$

$$V(T) \approx V_0[1 + \alpha_0(T-T_0) - 2\alpha_1(T^{1/2}-T_0^{1/2})] \approx V_0[1 + \alpha_0(T-T_0) - 20\alpha_0(T^{1/2}-T_0^{1/2})].$$

Fitting the V-T of pyrophyllite data reported in Table 1, we obtain:

$$\alpha_V(T_0) = 2.2(2)\cdot10^{-5}\ \text{K}^{-1} \text{ (with } V_0 = 424.2(1)\text{Å}^3 \text{ and } \alpha_0 = 5.5(3)\cdot10^{-5}\ \text{K}^{-1}).$$

Using the same formalism to describe the linear thermo-elastic behavior along the principal unit-cell axes, we obtained:

1) $\alpha_a(T_0) = 0.55(9)\cdot10^{-5}\ \text{K}^{-1}$ (with $a_0 = 5.152(2)$ Å and $\alpha_{0a} = 1.3(2)\cdot10^{-5}\ \text{K}^{-1}$);
2) $\alpha_b(T_0) = 0.46(12)\cdot10^{-5}\ \text{K}^{-1}$ (with $b_0 = 8.964(4)$ Å and $\alpha_{0b} = 1.1(3)\cdot10^{-5}\ \text{K}^{-1}$);
3) $\alpha_c((T_0) = 1.25(3)\cdot10^{-5}\ \text{K}^{-1}$ (with $c_0 = 9.352(1)$ Å and $\alpha_{0c} = 2.98(9)\cdot10^{-5}\ \text{K}^{-1}$)

The thermo-elastic anisotropy at 298 K can be described, at a first approximation, by α_a: α_b: α_c = 1.20 : 1 : 2.72.

A further description of volume and axial thermo-elastic behaviour based on a linear regression fit led to:

$$V(T)/V_0 = 1 + \alpha_{0V}\cdot T = 1 + 3.1(2)\cdot10^{-5}\cdot\Delta T;$$

$$a(T)/a_0 = 1 + \alpha_{0a}\cdot T = 1 + 7.3(4)\cdot10^{-6}\cdot\Delta T;$$

$$b(T)/b_0 = 1 + \alpha_{0b}\cdot T = 1 + 6.2(2)\cdot10^{-6}\cdot\Delta T;$$

$$c(T)/c_0 = 1 + \alpha_{0c}\cdot T = 1 + 16.6(2)\cdot10^{-6}\cdot\Delta T.$$

The magnitude and orientation of the principal unit-strain coefficients between room temperature and 623 K (*i.e.*, ΔT = 325 K), derived on the basis of the finite Eulerian strain tensor, were calculated using the following Cartesian axial system: x//a* and z//c. The strain ellipsoid is oriented as follows: $\varepsilon_3 = 0.0051(2)\ \text{K}^{-1}$, $\varepsilon_2 = 0.0022(3)\ \text{K}^{-1}$, and $\varepsilon_1 = 0.0015(3)\ \text{K}^{-1}$ (with $\varepsilon_3>\varepsilon_2>\varepsilon_1$); $\varepsilon_1\angle a = 40(11)°$, $\varepsilon_1\angle b = 50(10)°$, and $\varepsilon_1\angle c = 102(6)°$; $\varepsilon_2\angle a = 130(12)°$, $\varepsilon_2\angle b = 41(11)°$, and $\varepsilon_2\angle c = 90(8)$; $\varepsilon_3\angle a = 91(7)°$, $\varepsilon_3\angle b = 84(7)°$, and $\varepsilon_3\angle c = 12(9)°$. The orientation of the strain ellipsoid is shown in Fig. 1. The thermal anisotropy of pyrophyllite described on the basis of the unit-strain coefficients between 298 and 623 K is significant, with ε_1: ε_2: ε_3 = 1 : 1.47 : 3.40.

The evolution of the unit-cell paramaters of talc with T is shown in Fig. 3. At 423 K, the diffraction pattern was indexable with a monoclinic unit-cell (expected for the 2M-polytype), with a doubling of the c-axis (Table 1). At T > 1123 K, an irreversible transformation occurs, likely

ascribable to the first stage of the *T*-induced de-hydroxylation. Between 423 and 1123 K, the β angle decreases in response to the applied temperature; all the unit-cell edges show a monotonic increase (Table 1). The triclinic (1*Tc*) to monoclinic (2*M*) transition and the scattering of the data make it difficult to describe the axial thermal-expansion behavior (especially along [010] and [001]). The volume expansion coefficient of talc was modelled between 423 and 1123 K by a linear regression fit, as previously described for pyrophyllite data, yielding:
$V(T)/V_0 = 1 + \alpha_{0V} \cdot \Delta T = 1 + 2.15(3) \cdot 10^{-5} \cdot \Delta T$.

Discussion and conclusions

This is the first experiment in which the thermal and compressional behaviour of pyrophyllite-1*Tc* is described on the basis of in-situ H*P* single-crystal synchrotron diffraction and in-situ H*T* synchrotron powder diffraction, respectively. The previous experiment on the compressional behavior of talc-1*Tc* by Gatta et al. (2013), coupled with the thermal data obtained in this study, allow a comparative thermo-elastic analysis of the behaviour of pyrophyllite and talc. The EPMA-WDS chemical analysis reveals that the samples of pyrophyllite and talc used in this study approaches the ideal compositions [*i.e.*, $(Al_{1.94}Fe_{0.01})_{\Sigma 1.95}(Al_{0.07}Si_{3.93})_{\Sigma 4}O_{10}(OH)_{2.2}$ and $(Mg_{2.93}Fe_{0.06})_{\Sigma 2.99}(Al_{0.02}Si_{3.97})_{\Sigma 3.99}O_{10}(OH)_{2.10}$, respectively].

The high-pressure data of this study on pyrophyllite-1*Tc* up to 6.2 GPa leads to: K_{T0}= 47(3) GPa and *K'* = 6.6(14) for the M-EoS fit, K_{T0} = 54(1) GPa for the II-BM-EoS fit, and K_{T0}= 47(4) GPa and *K'* = 7.3(19) for a III-BM-EoS fit, with the following anisotropic compressional scheme: $\beta_a : \beta_b : \beta_c = 1.06 : 1 : 4.00$. The bulk modulus of pyrophyllite (refined as monoclinic, 2*M*) reported by Pawley et al. (2002), deduced by a M-EoS fit on the basis of powder diffraction data collected up to 6.3 GPa, is K_{T0}= 37(3) GPa with *K'* = 10(1), along with $\beta_a : \beta_b : \beta_c = 1.12 : 1 : 4.12$. We cannot exclude that the different elastic parameters (*i.e.*, K_{T0} and *K'*) obtained in this study and by Pawley et al (2002) are due to the different pyrophyllite polytypes used (*i.e.*, 1*Tc* and 2*M*, respectively) or, more likely, to the deviatoric stress observed by Pawley et al. (2002) in their experiment (as NaCl was used as *P*-transmitting medium). However, the anisotropic compressional schemes are in good agreement. Not surprisingly for a phyllosilicate, the compressibility along [100] and [010] are similar.

The thermal analysis (TG, DTG) of pyrophyllite-1*Tc* showed that this mineral is fully de-hydroxylated by 1120 K (see Guggheneim et al. 1987 for further details). The crystal structure of the de-hydroxylated pyrophyllite was reported by Wardle and Brindley (1972) and reviewed by Evans and Guggenheim (1988). The inter-layer stacking does not differ between the structure of pyrophyllite and its de-hydroxylated form, but the H*T*-induced transformation leads to a change of

the coordination environment of the Al site: from 6-fold to 5-fold. Consistently, our in-situ H*T* synchrotron powder diffraction experiment shows that pyrophyllite-1*Tc* is stable at least up to 700 K (Fig. 3, Table 1). Using the thermal equation of Pawley et al. (1996), we obtain for pyrophyllite-1*Tc* (at $T < 700$ K): $\alpha_0 = 5.5(3)\cdot10^{-5}$ K^{-1}. With the same equation, Pawley et al. (2002) obtained for pyrophyllite-2*M*: $\alpha_0 = 5.2\cdot10^{-5}$ K^{-1} (*esd* not given). The anisotropic thermal scheme obtained by Pawley et al. (2002) for monoclinic pyrophyllite was: $\alpha_a \sim \alpha_b < \alpha_c$ (*c*-axis is approximately twice as expandable as *a*- and *b*-axis), which agrees with the experimental findings of this study: α_a: α_b: α_c = 1.20 : 1 : 2.72. These findings suggest that the response of the two polytypes to the applied temperature is similar.

Despite the layered structure of pyrophyllite, the magnitude and orientation of the unit-strain ellipsoid in response to the applied pressure or temperature show that the highest compression or expansion directions are not perpendicular to the octahedral sheet, as $\varepsilon_3 \angle c$ = 19(1)° under hydrostatic compression and $\varepsilon_3 \angle c$ = 12(9)° at high temperature. Similar findings were reported by Gatta et al. (2013) on the compressional behaviour of talc-1*Tc*, where $\varepsilon_3 \angle c$ = 23.4(6)°.

The experimental results of Gatta et al. (2013) showed that talc-1*Tc* does not experience any phase transition if compressed hydrostatically at least up to 16 GPa. The compressional behavior of the unit-cell volume described with M-EoS and III-BM-EoS fits led to: K_{T0}= 57(3) GPa and *K'*= 4.9(5), and K_{T0}= 56(3)GPa and *K'*= 5.4(7), respectively. The anisotropic scheme, deduced on the basis of the axial compressibilities, was: $\beta_a : \beta_b : \beta_c = 1.03 : 1 : 3.15$.

The high-*T* behaviour of talc observed in this study shows that talc-1*T*c transforms to talc-2*M* at $T < 400$ K. Between 423 and 1123 K, we obtain a volume thermal expansion coefficient (by linear regression) of $2.15(3)\cdot10^{-5}$ K^{-1}, which is virtually identical to the value obtained (by linear regression) by Pawley et al. (1995) between 278-1083 K for talc-2*M*: $2.15(5)\cdot10^{-5}$ K^{-1}.

The comparative elastic analysis based on in-situ single-crystal X-ray diffraction experiments of pyrophyllite-1*Tc* (this study, M-Eos: K_{T0} = 47(3) GPa and *K'* = 6.6(14)) and talc (Gatta et al. 2013) (M-EoS: K_{T0}= 57(3) GPa and *K'*= 4.9(5)) shows that pyrophyllite is more compressible than talc. The volume thermal expansion coefficients obtained in this study by weighted linear regression through the *T*-*V* data points of pyrophyllite-1*Tc* (*i.e.*, $3.1(2)\cdot10^{-5}$, valid between 298-700 K) and talc-2*M* (*i.e.*, $2.15(3)\cdot10^{-5}$, valid between 423-1123 K) suggest that pyrophyllite is more expandable than talc.

The pronounced compressibility/expansivity perpendicular to T-O-T layer is expected to be mainly accommodated by the inter-layer van der Waals interactions, which are comparatively weaker than the intra-polyhedral bonds, making the structure of pyrophyllite or talc significantly less compressible on the *ab*-plane. The isothermal bulk moduli (and their *P*-derivatives) and the

isobaric expansion coefficients of pyrophyllite and talc obtained in this study and by Gatta et al. (2013) show that the *P*-induced compressibility and the *T*-induced expansivity of these two phyllosilicates are similar to those of micas (Zanazzi and Pavese 2002 for a review). Despite the lack of H*P*/H*T*-structure refinements in this study prevents the description of the deformation mechanisms at the atomic level in response to the applied pressure/temperature, we can expect that the ditrigonal distortion is probably the most *P*/*T*-induced energy-convenient mechanism in pyrophyllite and talc to make octahedral- and tetrahedral-sheets match one another so as to form the T-O-T layer, as observed in micas (*e.g.*, Gatta et al. 2009, 2010, 2011, 2012; Zanazzi and Pavese 2002). However, the absence of inter-layer cations in pyrophyllite and talc structures, which were proven to influence significantly the ditrigonal distortion mechanisms, leaves several open questions about the actual main deformation mechanisms.

If we combine the thermo-elastic parameters obtained in this study and those reported by Gatta et al. (2013), *P*-*T*-*V* EoS of pyrophyllite and talc (valid at a first approximation) can be obtained:

Pyrophyllite: $V_{(P,T)} \sim V_{(P0,T0)}[1 - \beta\Delta P + \alpha\Delta T] = V_{(P0,T0)}[1 - 0.021(1)\cdot\Delta P + 3.1(2)\cdot10^{-5}\cdot\Delta T]$;

Talc : $V_{(P,T)} \sim V_{(P0,T0)}[1 - \beta\Delta P + \alpha\Delta T] = V_{(P0,T0)}[1 - 0.018(1)\cdot\Delta P + 2.15(3)\cdot10^{-5}\cdot\Delta T]$

(with $\beta = 1/K_{T0}$ in GPa^{-1} and α in K^{-1}).

Acknowledgements

Parts of this research were carried out at the light source PETRA III at DESY, a member of the Helmholtz Association (HGF). The authors also thank ELETTRA (Trieste, Italy) for the allocation of synchrotron beam time. GDG, PL, MM and AP thank the Italian Ministry of Education, MIUR-Project: 2010EARRRZ_003. The Editor Milan Rieder, Wilson Crichton and an anonymous reviewer are thanked.

References

Agilent (2012) Xcalibur CCD system, CrysAlis Software system.

Angel RJ (2000) Equation of State. In R.M. Hazen, R.T. Downs, Eds., High-Temperature and High-Pressure Crystal Chemistry, Reviews in Mineralogy and Geochemistry, Vol. 41, pp 35-59. Mineralogical Society of America and Geochemical Society, Washington, DC, U.S.A..

Angel RJ (2011) Win_Strain V4.11. Computer program (http://www.rossangel.com/).

Angel RJ, Bujak M, Zhao J, Gatta GD, Jacobsen SD (2007) Effective hydrostatic limits of pressure media for high-pressure crystallographic studies. J Appl Crystallogr 40:26–32.

Bailey SW (1988) Introduction; Polytypism of 1:1 layer silicates. In S.W. Bailey, Ed., Hydrous Phyllosilicates (Exclusive of Micas), Review in Mineralogy, Vol. 19, p. 1–27. Mineralogical Society of America, Washington, DC, U.S.A.

Birch F (1947) Finite elastic strain of cubic crystal. Phys Rev 71:809-824.

Boehler R, De Hantsetters K (2004) New anvil designs in diamond-cells. High Pressure Res 24:391-396.

Dellisanti F, Valdrè G (2008) Linear relationship between thermo-dehydroxylation and induced-strain by mechanical processing in vacuum: The case of industrial kaolinite, talc and montmorillonite. Int J Miner Process 88:94-99.

Dellisanti F, Valdrè G (2010) On the high-temperature structural behaviour of talc ($Mg_3Si_4O_{10}(OH)_2$) to 1600°C: Effect of mechanical deformation and strain. Phil Mag 90:2443–2457.

Dellisanti F, Valdrè G, Mondonico M (2009) Changes of the main physical and technological properties of talc due to mechanical strain. Appl Clay Sci 42:398-404.

Ďurovič S, Weiss Z (1983) Polytypism of pyrophyllite and talc. Part I. OD interpretation and MDO polytypes. Silikáty 27:1-8.

Evans BW, Guggenheim S (1988) Talc, pyrophyllite, and related minerals. In S.W. Bailey, Ed., Hydrous Phyllosilicates (Exclusive of Micas), Review in Mineralogy, Vol. 19, p. 225– 294. Mineralogical Society of America, Washington, DC, U.S.A.

Gatta GD, Rotiroti N, Pavese A, Lotti P, Curetti N (2009) Structural evolution of a 3*T* phengite mica up to 10 GPa: an in-situ single-crystal X-ray diffraction study. Z Kristallogr 224:302-310.

Gatta GD, Rotiroti N, Lotti P, Pavese A, Curetti N (2010) Structural evolution of a 2M_1 phengite mica up to 11 GPa: an in-situ single-crystal X-ray diffraction study. Phys Chem Minerals 37:581-591.

Gatta GD, Merlini M, Rotiroti N, Curetti N, Pavese A (2011) On the crystal chemistry and elastic behavior of a phlogopite 3*T*. Phys Chem Minerals 38:655-664.

Gatta GD, Merlini M, Liermann H-P, Rothkirch A, Gemmi M. Pavese A (2012) The thermoelastic behavior of clintonite up to 10 GPa and 1,000°C. Phys Chem Minerals 39:385-397.

Gatta GD, Merlini M, Valdrè G, Liermann H-P, Nénert G, Rothkirch A, Kahlenberg V, Pavese A (2013) On the crystal structure and compressional behaviour of talc: a mineral of interest in petrology and material science. Phys Chem Minerals 40:145-156.

Guggenheim S, Chang HY, Koster van Groos AF (1987) Muscovite dehydroxylation: High-temperature studies. Am Mineral 72:537–550.

Holland TJB, Powell R (1998) An internally consistent thermodynamic data set for phases of petrological interest. J Metamorphic Geol 16:309-343.

Holland TJB, Redfern SAT (1997) Unit cell refinement from powder diffraction data: the use of regression diagnostics. Min Mag 61: 65-77.

Larson AC, Von Dreele RB (2004) General Structure Analysis System (GSAS), Los Alamos National Laboratory Report LAUR, pp. 86-748.

Le Bail A, Duroy H, Fourquet JL (1988) Ab-initio structure determination of $LiSbWO_6$ by X-ray powder diffraction. Mat Res Bull 23:447-452.

Lee JH, Guggenheim S (1981) Single crystal X-ray refinement of pyrophyllite-1*Tc*. Am Mineral 66:350-357.

Mao HK, Xu J, Bell PM (1986) Calibration of the ruby pressure gauge to 800 kbar under quasi-hydrostatic conditions. J Geophys Res 91:4673-4676.

Murnaghan FD (1937) Finite deformations of an elastic solid. Am J Math 49:235-260.

Mysen BO, Ulmer P, Konzett J, Schmidt MW (1998) The upper mantle near convergent plate boundaries. In R.J. Hemley, Ed., Ultrahigh-Pressure Mineralogy: Physics and Chemistry of the Earth's Deep Interior, Review in Mineralogy, Vol. 37, p. 97–138. Mineralogical Society of America, Washington, DC, U.S.A.

Pawley AR, Wood BJ (1995) The high-pressure stability of talc and 10 Å phase: potential storage sites for H2O in subduction zones. Am Mineral 80:998–1003.

Pawley AR, Redfern SAT, Wood BJ (1995) Thermal expansivities and compressibilities of hydrous phases in the system MgO-SiO_2-H_2O: Talc, phase A and 10-angstrom phase. Contrib Mineral Petrol 122:301–307.

Pawley AR, Redfern SAT, Holland TJB (1996) Volume behaviour of hydrous minerals at high pressure and temperature: 1. Thermal expansion of lawsonite, zoisite, clinozoisite, and diaspore. Am Mineral 81:335-340.

Pawley AR, Clark SM, Chinnery NJ (2002) Equation of state measurements of chlorite, pyrophyllite, and talc. Am Mineral 87:1172–1182.

Poli S, Schmidt MW (2002) Petrology of Subducted Slabs. Annual Review of Earth and Planetary Sciences 30:207–235.

Rietveld HM (1969) A profile refinement method for nuclear and magnetic structures. J Appl Crystallogr 2:65–71.

Rothkirch A, Gatta GD, Meyer M, Merkel S, Merlini M, Liermann H-P (2013) Single-crystal diffraction at the Extreme Conditions beamline P02.2: procedure for collecting and analyzing high-pressure single-crystal data. J Synchrotron Rad 20:711 – 720.

Symmes GH (1986) The thermal expansion of natural muscovite, paragonite, margarite, pyrophyllite, phlogopite, and two chlorites: the significance of high *T/P* volume studies on calculated phase equilibria. B. A. Thesis, Amherst College, Amherst, Massachusetts.

Thomson P, Cox DE, Hastings JB (1987) Rietveld refinement of Debye-Scherrer synchrotron X-ray data from Al_2O_3. J Appl Crystallogr 20:79-83.

Theye T, Chopin C, Grevel KD, Ockenga E (1997) The assemblage diaspore + quartz in metamorphic rocks: a petrological, experimental and thermodynamic study. J Metamorph Geol 15:17–28.

Ulian G, Tosoni S, Valdrè G (2014) The compressional behaviour and the mechanical properties of talc [$Mg_3Si_4O_{10}(OH)_2$]: a density functional theory investigation. Phys Chem Minerals 41:639-650.

Wardle R, Brindley GW (1972) The crystal structure of pyrophyllite, 1*Tc*, and of its dehydroxilate. Am Mineral 57:732-750.

Weiss Z, Ďurovič S (1984) Polytypism of pyrophyllite and talc. Silikáty 28:289-309.

Zanazzi PF, Pavese A (2002) Behavior of micas at high pressure and high temperature. In A. Mottana, F.P. Sassi, J.B. Thompson, Jr., S. Guggenheim, Eds., Micas: Crystal Chemistry and Metamorphic Petrology, Review in Mineralogy and Geochemistry, Vol. 46, p. 99-116. Mineralogical Society of America and Geochemical Society, Washington, DC, U.S.A..

Figure 1. (*Left side*) A view of crystal structure of pyrophyllite (perpendicular to the *ac* plane) and orientation of the unit-strain ellipsoids with ΔP = 6.2 GPa (light blue) and ΔT = 325 K (yellow), based on the experimental findings of this study. (*Right side*) Clinographic view of the layered structure of pyrophyllite.

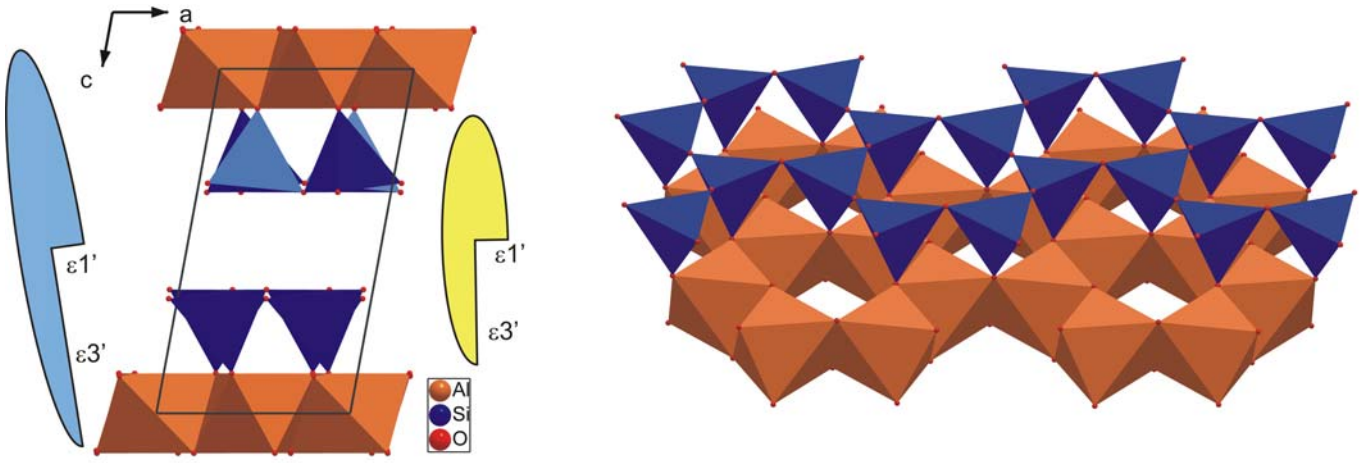

Figure 2. Evolution of the unit-cell parameters of pyrophyllite with pressure; the solid lines represent the BM-EoS fit for the *a*, *b* and *c*-axis and for the unit-cell volume (see text for details) and the weighted linear regression through the data points for the α, β and γ angles. Evolution of the "normalized stress" ($Fe = P/[3fe(1+2fe)^{5/2}]$) *vs.* Eulerian finite strain ($fe= [(V_0/V)^{2/3} - 1]/2$); the solid line is a weighted linear fit through the data.

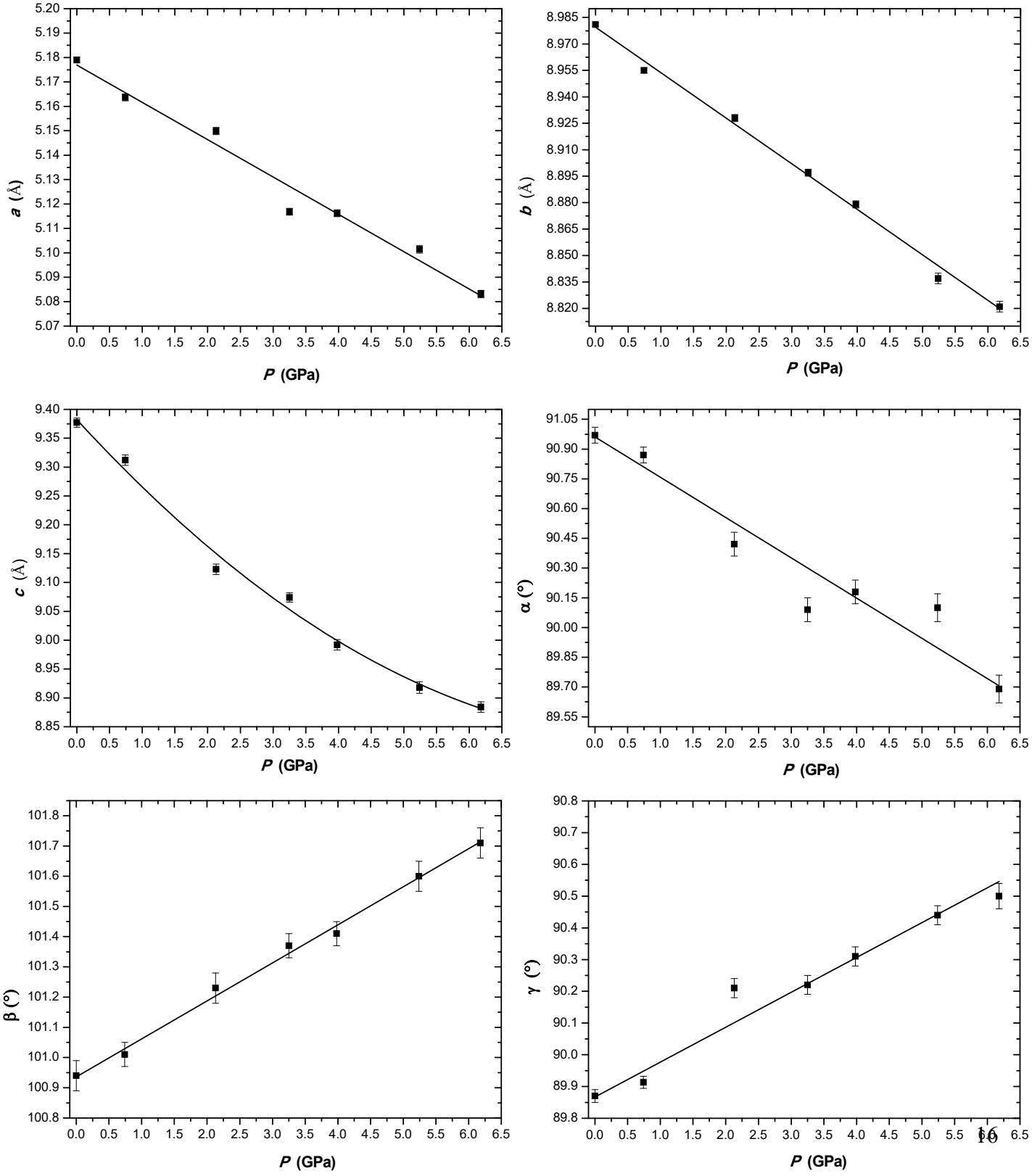

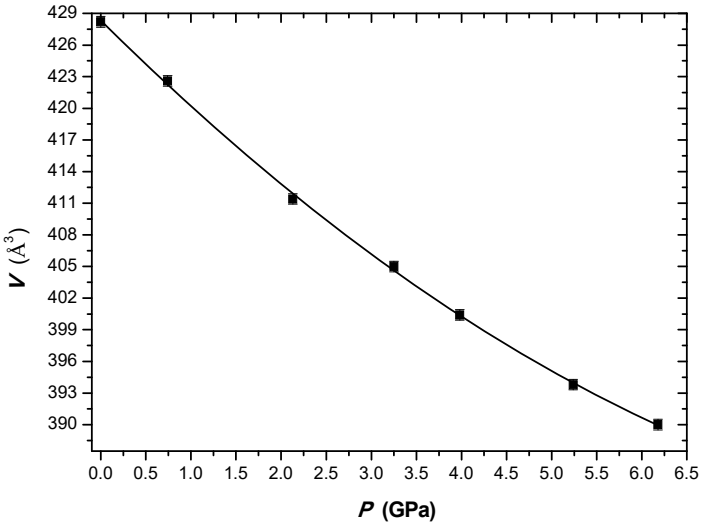
V (Å3)
P (GPa)

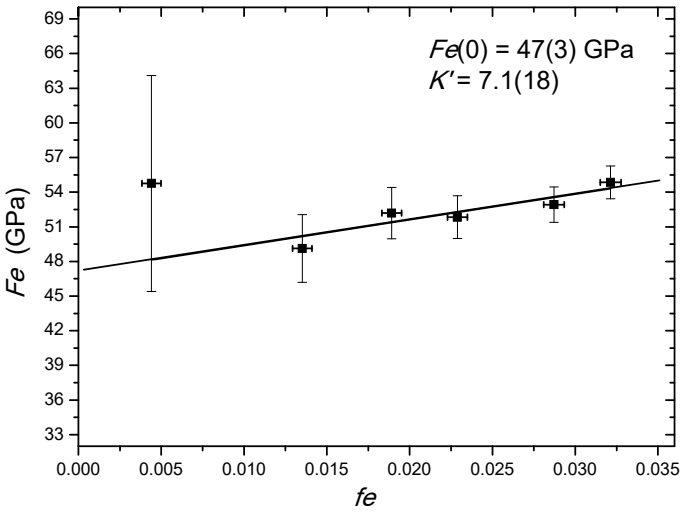
Fe(0) = 47(3) GPa
K′ = 7.1(18)
Fe (GPa)
fe

Figure 3. Evolution with T of the unit-cell parameters of pyrophyllite-1*Tc* and of the unit-cell volume of the monoclinic polymorph of talc (2*M*, $T > 400$ K). The solid lines (in red) represent the Pawley et al. (1996) thermal equation fit for pyrophyllite-1*Tc* ($298<T<773$) and the weighted linear regression through the data points for talc-2*M* ($423<T<1123$).

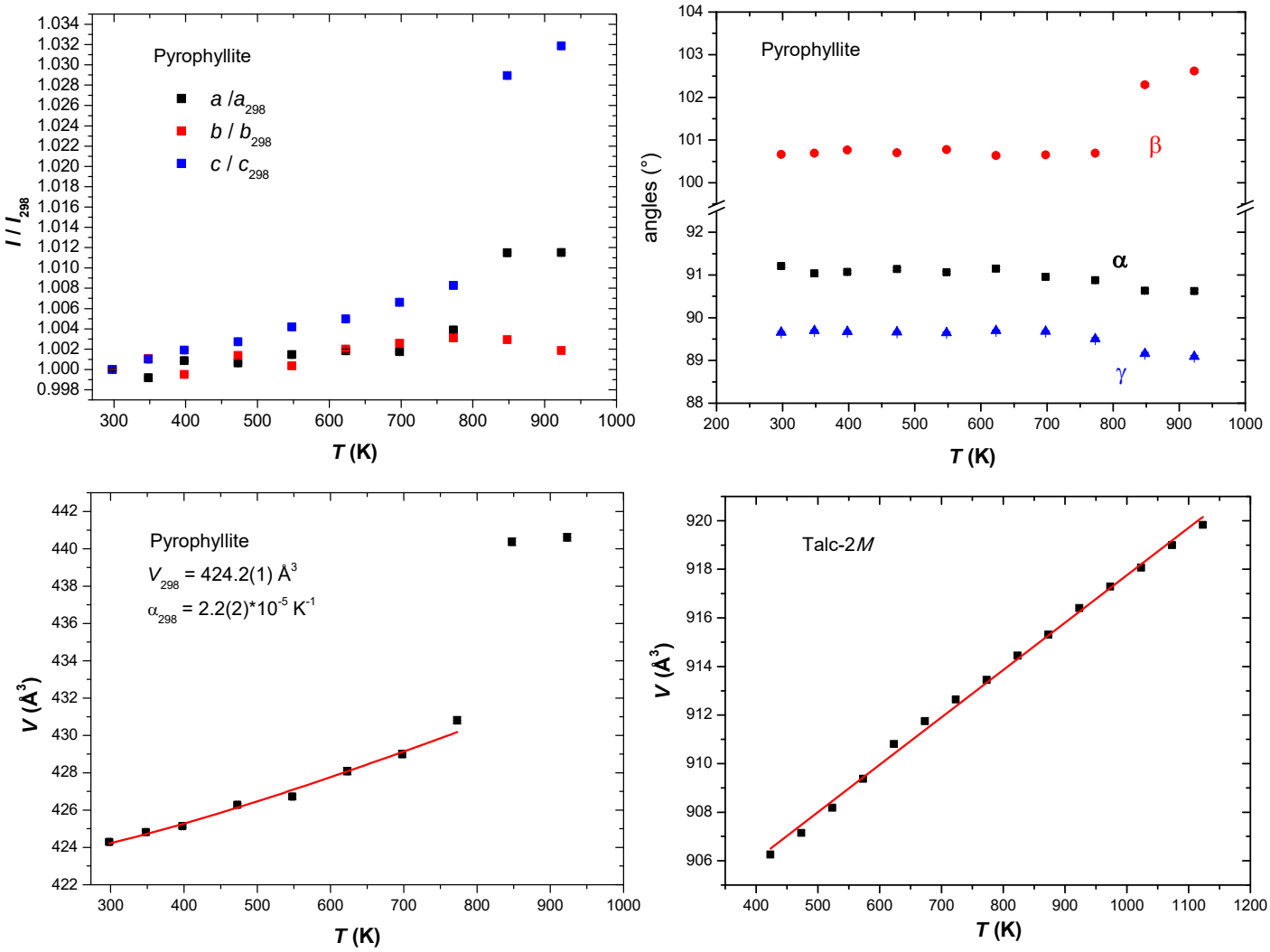

Table 1. Unit-cell parameters of pyrophyllite at high *P* and high *T* and of talc at high *T* based on the experimental findings of this study.

P (GPa) Pyrophyllite	*a* (Å)	*b* (Å)	*c* (Å)	α (°)	β (°)	γ (°)	*V* (Å^3)
0.0001	5.179(1)	8.981(1)	9.377(8)	90.97(4)	100.94(5)	89.87(2)	428.2(5)
0.74(8)	5.164(1)	8.955(1)	9.312(8)	90.87(4)	101.01(4)	89.91(2)	422.6(5)
2.13(8)	5.150(1)	8.928(2)	9.123(8)	90.42(6)	101.23(5)	90.21(3)	411.4(5)
3.25(8)	5.117(1)	8.897(2)	9.074(8)	90.09(6)	101.37(4)	90.22(3)	405.0(5)
3.98(8)	5.116(1)	8.879(2)	8.992(9)	90.18(6)	101.41(4)	90.31(3)	400.4(6)
5.24(8)	5.101(1)	8.837(2)	8.918(9)	90.10(7)	101.60(5)	90.44(3)	393.8(6)
6.18(8)	5.083(1)	8.821(3)	8.884(9)	89.69(7)	101.71(5)	90.50(4)	390.0(6)
T (K) Pyrophyllite							
298(2)	5.1533(7)	8.9629(8)	9.3497(9)	91.21(3)	100.66(3)	89.66(2)	424.3(1)
348(2)	5.1491(8)	8.9724(9)	9.359(1)	91.04(3)	100.69(3)	89.69(2)	424.8(1)
398(2)	5.1577(8)	8.9585(9)	9.367(1)	91.07(3)	100.77(3)	89.67(2)	425.1(1)
473(2)	5.1566(9)	8.9753(9)	9.375(1)	91.14(3)	100.70(3)	89.66(2)	426.3(1)
548(2)	5.1609(8)	8.9661(9)	9.389(1)	91.06(3)	100.78(3)	89.64(2)	426.7(1)
623(2)	5.1628(8)	8.9807(9)	9.396(1)	91.15(3)	100.64(3)	89.69(2)	428.1(2)
698(2)	5.1624(9)	8.9860(9)	9.411(1)	90.96(3)	100.65(3)	89.68(2)	429.0(2)
773(2)	5.1733(9)	8.991(1)	9.427(1)	90.88(3)	100.69(3)	89.50(3)	430.8(2)
848(2)	5.212(1)	8.989(1)	9.620(1)	90.63(4)	102.29(4)	89.16(3)	440.4(2)
923(2)	5.213(1)	8.980(1)	9.648(2)	90.63(4)	102.61(4)	89.09(3)	440.6(2)
T (K) Talc							
298(2)	5.2877(8)	9.1587(7)	9.4654(8)	90.63(3)	99.53(3)	90.07(2)	452.0(1)
323(2)	5.2896(8)	9.1583(8)	9.4643(8)	90.59(3)	99.34(3)	90.07(3)	452.4(1)
348(2)	5.2906(8)	9.1584(8)	9.4629(8)	90.52(3)	99.19(3)	90.08(2)	452.6(1)
373(2)	5.2902(8)	9.1593(8)	9.4549(9)	90.38(4)	98.79(3)	90.12(3)	452.7(2)
423(2)	5.2893(8)	9.1639(8)	18.908(2)	90	98.57(3)	90	906.3(4)
473(2)	5.2912(8)	9.1639(9)	18.907(2)	90	98.31(3)	90	907.1(4)
523(2)	5.2926(8)	9.1655(8)	18.907(2)	90	98.03(4)	90	908.2(4)
573(2)	5.2953(8)	9.1651(8)	18.909(2)	90	97.74(3)	90	909.4(4)
623(2)	5.2980(8)	9.1649(8)	18.921(2)	90	97.53(3)	90	910.8(4)
673(2)	5.2999(9)	9.1659(8)	18.927(2)	90	97.41(3)	90	911.7(4)
723(2)	5.3007(8)	9.1678(9)	18.934(2)	90	97.30(3)	90	912.6(4)
773(2)	5.3029(9)	9.1676(8)	18.938(2)	90	97.19(3)	90	913.4(4)
823(2)	5.3045(9)	9.1691(9)	18.946(2)	90	97.08(3)	90	914.4(4)
873(2)	5.3054(9)	9.1700(9)	18.956(2)	90	97.02(3)	90	915.3(4)
923(2)	5.307(1)	9.1711(9)	18.968(2)	90	96.94(4)	90	916.4(4)
973(2)	5.310(1)	9.170(1)	18.974(2)	90	96.89(4)	90	917.3(5)
1023(2)	5.311(1)	9.172(1)	18.982(2)	90	96.86(3)	90	918.1(4)
1073(2)	5.313(1)	9.173(1)	18.990(3)	90	96.78(4)	90	918.9(6)
1123(2)	5.315(1)	9.172(1)	18.998(3)	90	96.72(4)	90	919.8(6)
1173(2)	5.324(2)	9.165(3)	18.994(5)	90	96.49(6)	90	920.8(9)